arXiv:1011.2472v1 [astro-ph.GA] 10 Nov 2010

1.3 mm WAVELENGTH VLBI OF SAGITTARIUS A*: DETECTION OF TIME-VARIABLE EMISSION ON EVENT HORIZON SCALES

Vincent L. Fish[1], Sheperd S. Doeleman[1], Christopher Beaudoin[1], Ray Blundell[2], David E. Bolin[1,3], Geoffrey C. Bower[4], Richard Chamberlin[5], Robert Freund[6], Per Friberg[7], Mark A. Gurwell[2], Mareki Honma[8], Makoto Inoue[9], Thomas P. Krichbaum[10], James Lamb[11], Daniel P. Marrone[12,13], James M. Moran[2], Tomoaki Oyama[8], Richard Plambeck[4], Rurik Primiani[2], Alan E. E. Rogers[1], Daniel L. Smythe[1], Jason SooHoo[1], Peter Strittmatter[6], Remo P. J. Tilanus[7,14], Michael Titus[1], Jonathan Weintroub[2], Melvyn Wright[4], David Woody[11], Ken H. Young[2], Lucy M. Ziurys[6]
Draft version November 11, 2010

ABSTRACT

Sagittarius A*, the $\sim 4 \times 10^6 \, M_\odot$ black hole candidate at the Galactic Center, can be studied on Schwarzschild radius scales with (sub)millimeter wavelength Very Long Baseline Interferometry (VLBI). We report on 1.3 mm wavelength observations of Sgr A* using a VLBI array consisting of the JCMT on Mauna Kea, the ARO/SMT on Mt. Graham in Arizona, and two telescopes of the CARMA array at Cedar Flat in California. Both Sgr A* and the quasar calibrator 1924−292 were observed over three consecutive nights, and both sources were clearly detected on all baselines. For the first time, we are able to extract 1.3 mm VLBI interferometer phase information on Sgr A* through measurement of closure phase on the triangle of baselines. On the third night of observing, the correlated flux density of Sgr A* on all VLBI baselines increased relative to the first two nights, providing strong evidence for time-variable change on scales of a few Schwarzschild radii. These results suggest that future VLBI observations with greater sensitivity and additional baselines will play a valuable role in determining the structure of emission near the event horizon of Sgr A*.

Subject headings: Galaxy: center — submillimeter: general — techniques: high angular resolution — techniques: interferometric

1. INTRODUCTION

The case for linking Sgr A*, the radio source at the center of the Milky Way, with a supermassive black hole is very strong. Mass estimates inferred from stellar orbits, proper motion studies that indicate Sgr A* is nearly motionless, VLBI observations that reveal it is ultracompact, and short-timescale variability from radio to X-rays all point towards Sgr A*'s association with a $\sim 4 \times 10^6 \, M_\odot$ black hole (Reid 2009, and references therein). At a distance of ~ 8 kpc, the Schwarzschild radius of this black hole subtends $R_{\text{Sch}} \sim 10 \, \mu$as, making the

vfish@haystack.mit.edu

[1] Massachusetts Institute of Technology, Haystack Observatory, Route 40, Westford, MA 01886, USA
[2] Harvard-Smithsonian Center for Astrophysics, 60 Garden St., Cambridge, MA 02138, USA
[3] University of Arizona, Tucson AZ, 85721, USA
[4] University of California Berkeley, Dept. of Astronomy, Radio Astronomy Laboratory, 601 Campbell, Berkeley, CA 94720-3411, USA
[5] Caltech Submillimeter Observatory, 111 Nowelo St., Hilo, HI 96720, USA
[6] Arizona Radio Observatory, Steward Observatory, University of Arizona, 933 North Cherry Ave., Tucson, AZ 85721-0065, USA
[7] James Clerk Maxwell Telescope, Joint Astronomy Centre, 660 North A'ohoku Place, University Park, Hilo, HI 96720, USA
[8] National Astronomical Observatory of Japan, Osawa 2-21-1, Mitaka, Tokyo 181-8588, Japan
[9] Institute of Astronomy and Astrophysics, Academia Sinica, P.O. Box 23-141, Taipei 10617, Taiwan
[10] Max-Planck-Institut für Radioastronomie, Auf dem Hügel 69, D-53121 Bonn, Germany
[11] OVRO, California Institute of Technology, 100 Leighton Lane, Big Pine, CA 93513-0968, USA
[12] Kavli Institute for Cosmological Physics, University of Chicago, 5640 South Ellis Avenue, Chicago, IL 60637, USA
[13] Hubble Fellow
[14] Netherlands Organization for Scientific Research, Laan van Nieuw Oost-Indie 300, NL2509 AC The Hague, The Netherlands

apparent size of its event horizon the largest that we know of. VLBI at (sub)millimeter wavelengths is ideally suited to observing Sgr A* on these angular scales. Previous 1.3 mm VLBI detections of Sgr A* on a Hawaii-Arizona baseline established the existence of coherent structures on scales of a few R_{Sch} (Doeleman et al. 2008).

Current 1.3 mm VLBI observations can be used to address two fundamental questions concerning the nature of Sgr A*. The first is whether the accretion flow surrounding Sgr A* exhibits an expected "shadow" feature that occurs due to the strong gravitational lensing near the black hole. Emission from the accretion flow is preferentially lensed onto the last photon orbit, resulting in a relatively dim central region encircled by a brighter annulus (Falcke et al. 2000). A second question is whether the flaring behavior exhibited by Sgr A* has its origins in compact structures that arise near the black hole event horizon. Broadband flares on timescales ranging from minutes to hours are well-documented (Marrone et al. 2008; Yusef-Zadeh et al. 2009; Dodds-Eden et al. 2009) and imply time-variable structures in the innermost accretion region. If small-scale variable structures are present, 1.3 mm VLBI can sensitively monitor the changing morphology of Sgr A* using non-imaging techniques with time resolutions of tens of seconds (Doeleman et al. 2009; Fish et al. 2009b).

We report on new 1.3 mm VLBI observations of Sgr A* using a four-telescope array. These observations confirm event horizon scale structure within Sgr A*, impose new constraints on accretion models for Sgr A*, and reveal time-dependent variability on scales of a few R_{Sch}.

2. OBSERVATIONS

Sgr A* and several calibrator sources were observed with four telescopes at three observatories: the James Clerk Maxwell Telescope (JCMT; henceforth also J) on Mauna Kea

in Hawaii, the Arizona Radio Observatory's Submillimeter Telescope (ARO/SMT; S) in Arizona, and two telescopes of the Combined Array for Research in Millimeter-wave Astronomy (CARMA; C and D, located ~ 60 m apart) in California. On Mauna Kea, the Submillimeter Array (SMA) housed the VLBI recording system and synthesized the hydrogen maser based VLBI reference used at the JCMT. Masers at all sites were checked against ultra-stable crystals; combined losses due to maser instabilities and local oscillator decoherence are estimated to be $\lesssim 5\%$. Observations occurred over three nights: 2009 April 5–7 (days 95–97). Sources were observed in left circular polarization in two 480 MHz bandwidths centered at 229.089 and 229.601 GHz (low and high bands). Data recorded at all sites was shipped to MIT Haystack Observatory in Westford, Massachusetts for processing on the Mark4 VLBI correlator. Once correlated, data for each scan (typically 10–15 minutes) were corrected for coherence losses due to atmospheric turbulence and searched for detections using methods detailed in Doeleman et al. (2001, 2008). Atmospheric coherence times ranged from a few to ~ 20 s, depending on weather conditions at each telescope.

3. CALIBRATION

The VLBI correlation coefficient for each baseline was multiplied by the geometric mean of the System Equivalent Flux Density (SEFD) of both antennas. The SEFD is a product of antenna gain (Jy/K) and the opacity-corrected system temperature, which was measured just prior to each VLBI scan using a vane calibration technique that corrects for the atmosphere. For the JCMT and ARO/SMT, antenna gains were determined from observations of planets at several points during the multiple day campaign, and the gains were observed to be stable. Relative gains for the two CARMA dishes were estimated using observations taken by CARMA in interferometric array mode before each VLBI scan, and the gains were then set to a common flux scale using planet scans at the end of each night.

The flux densities of all VLBI targets (Sgr A*, 1924−292, M87, 3C273, 3C345, 1733−130, 3C279, 0854+201) were measured with CARMA. For Sgr A*, data with baselines shorter than 20 kλ were discarded to filter out extended emission in the Galactic center. The measured flux densities of all sources increased from day 95 to day 96 and from day 96 to day 97. We attribute this systematic trend to errors in the planet calibrations made shortly after sunrise, when antenna focus, pointing offsets, and atmospheric coherence typically change. The flux density measured for the calibrator 1924−294, observed over the same time and elevation ranges as Sgr A*, was 9.95, 10.21, and 10.75 Jy on days 95, 96, and 97. We normalized CARMA gains to a constant flux density of 10.25 Jy on all three days. The resulting measured flux densities for Sgr A* are 3.03, 3.16, and 3.61 Jy on days 95, 96, and 97, respectively. We adopt these fluxes for all subsequent analysis.

As shown in the upper panels of Figures 1 and 2, there are still noticeable variations in the correlated flux densities even after renormalizing the day-to-day flux scales. These residual calibration errors and amplitude variation can be corrected for by making three simplifying assumptions that allow us to use standard "self-calibration" techniques. First, the flux densities of detections in the low and high bands, which differ by only 0.2% in frequency, are assumed to be equal in each scan. Second, flux densities on the SC and SD baselines are assumed to be equal. While one could in principle require that JC and

JD flux densities be equal as well, the signal-to-noise ratio (SNR) is generally much lower on the JC and JD baselines than on the shorter VLBI baselines (SC and SD), since both 1924−292 and Sgr A* are more resolved on longer baselines. Third, CARMA antenna gains are adjusted to make the correlated flux density on the CD baseline (with a fringe spacing measured in arcseconds) equal to the total flux density measured each night by CARMA. This final constraint enforces a constant source flux density over the duration of each night of observation. While some of the observed variation in Sgr A* over the course of a night may be due to intrinsic variability, the 1924−292 data exhibit similar scatter, suggesting that calibration errors may dominate over source variability. Combined, these assumptions result in a closed-form solution for gain-correction coefficients for telescopes C, D, and S in each band. Henceforth, we will use the term "gain-corrected" to refer to flux densities that have been multiplied by these gain-correction coefficients. We note that if the total flux density (CD) is varied, the SJ flux densities are unchanged while other flux densities vary as the square root of the factor.

The quasar 1924−292 was easily detected on all baselines (Table 1). On each scan, low-band and high-band fluxes after a-priori calibration track each other consistently (Figure 1). After gain correction assuming a total flux density of 10.25 Jy, the data from all three days are highly consistent with one another. The SC and SD baselines show consistent variation in the correlated flux density that is repeated each day. The long-baseline detections (SJ, JC, and JD) also show day-to-day repeatable behavior, indicating detection of stable source structure presumably associated with a jet (Shen 1997). The consistency of these data demonstrates the validity of the gain-correction technique. Based on the statistics of the data on scans of 1924−292, systematic errors are estimated to be $\sim 5\%$.

4. RESULTS

We report the first 1.3 mm VLBI detections of Sgr A* on Hawaii-California baselines with correlated flux densities for several scans of $\gtrsim 400$ mJy on the JC and JD baselines during day 96 (Figure 2). Nondetections on the JC and JD baselines on day 95 are attributable to the higher opacity at the JCMT on that day. The robust detections on the long (Hawaii-Arizona and Hawaii-California) baselines confirm the detection of event horizon scale structure reported in Doeleman et al. (2008).

Because Sgr A* was detected on baselines between all three sites, we are able to measure closure phase: the sum of interferometric phase around a closed triangle of baselines. This quantity is relatively immune to calibration errors and in general provides important constraints on source structure. On the CARMA-ARO/SMT-JCMT triangle, the phase closures on Sgr A* for day 96 (5 independent measurements) were computed using 10-second coherent integrations, which were averaged over full 10-minute VLBI scans to increase SNR (Rogers et al. 1995). Because of the relatively low SNR on the long baselines to the JCMT, it is only possible to say that the closure phases are consistent with a value of zero with a variation of $\pm 40°$.

4.1. *Variability*

The arcsecond-scale flux density of Sgr A* on days 95 and 96 is the same to within uncertainties in the flux scale, but on day 97 the flux density of Sgr A* was $\sim 17\%$ higher. This
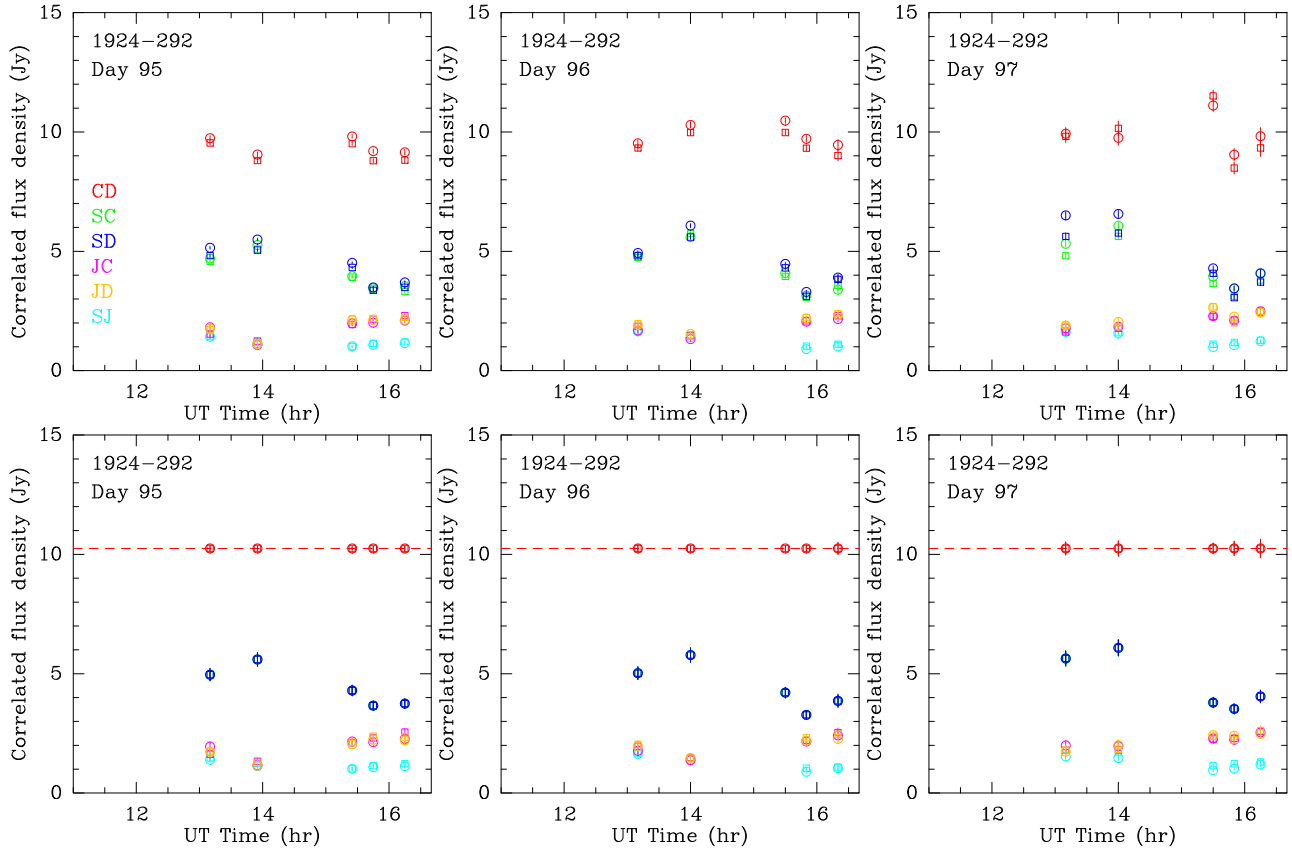
FIG. 1.— *Top*: Observations of 1924−292. Detections are color-coded by baseline. Squares indicate low-band data and circles indicate high-band data. The day 97 a-priori calibration is noticeably poorer at CARMA. *Bottom*: Same, after gain correction. Errorbars include a 5% systematic component. The gain-corrected data exhibit much higher day-to-day repeatability. The red dashed line shows the assumed CD flux (the associated flux scale uncertainty is ∼ 5%, modulo uncertainties in planet fluxes). Gain-corrected SC and SD data are equal by definition.

brightening is accompanied by changes on VLBI scales as well. First, the SC/CD and SD/CD flux density ratios are higher on day 97 than on days 95 and 96 (Figure 2). Second, there are more Hawaii-California detections during day 97, and the apparent flux densities on these baselines are on average higher than on day 96. Third, the flux densities on the SJ baseline are also larger on day 97. These differences are consistent with an episode of variability in Sgr A* during which the small-scale structure increased in flux density between days 96 and 97.

4.2. *Geometrical Models of the Structure of Sgr A*

Though our data are better calibrated than in the previous epoch (Doeleman et al. 2008), the structure of Sgr A* is poorly constrained because millimeter VLBI detections of Sgr A* remain limited in terms of baseline length and orientation. As a result, many models can be made to fit the data: extended double sources, large rings, combinations of large- and small-scale components, etc.

Nevertheless, with the caveat that this small dataset should not be overinterpreted, it is instructive to investigate the two classes of models originally considered by Doeleman et al. (2008) to fit the 1.3 mm VLBI data obtained in 2007: circular Gaussians and rings. All of the 2007 data points could be fitted by a single Gaussian component. In contrast, we note a loss of ∼ 1 Jy of correlated flux density between the connected-element (CD) and SC/SD baselines (Figure 3). In the context of Gaussian models of emission on $R_{\rm Sch}$ scales, this suggests the existence of additional variable structure on

scales between those probed by the SC/SD (a few hundred microarcseconds) and the CD (a few arcseconds) baselines.

We adopt this assumption to estimate the size of the inner accretion flow in Sgr A*. Effectively, this reduces to fitting all of the VLBI data excluding the CD data points. For the Gaussian model, the best fits imply a flux density of $2.07^{+0.14}_{-0.15}$ Jy and a size of $41.3^{+5.4}_{-4.3}$ μas (FWHM; errors are 3σ) on day 95 and $2.07^{+0.19}_{-0.19}$ Jy and $44.4^{+3.0}_{-3.0}$ μas on day 96 (Figure 3 and Table 2). These values are consistent with the single compact component Gaussian fit of Doeleman et al. (2008), who estimated a flux density of 2.4 ± 0.5 Jy and a size of 43^{+14}_{-8} μas (before deconvolution of the expected interstellar scattering; 37 μas unscattered) for the 230 GHz emission. On day 97, the best fit model has a much higher flux density of $2.85^{+0.29}_{-0.28}$ Jy but a similar FWHM of $42.6^{+3.1}_{-2.9}$ μas. Despite the increase in flux density observed on day 97, the diameter of the fitted compact component in Sgr A* on that day is identical (to within the errors) to the values for the size obtained on days 95 and 96.

Ring models with three parameters (inner radius, outer radius, and flux density) can also fit the VLBI data (Figure 3 and Table 2). However, no single set of ring model parameters consistently fits the data on all three days, which would suggest that the size and structure of Sgr A* are variable within the context of ring models. This stands in contrast with the Gaussian model, for which all epochs of data are consistent with a uniform size despite differences in the flux density. Longer-wavelength VLBI observations are inconclusive as to
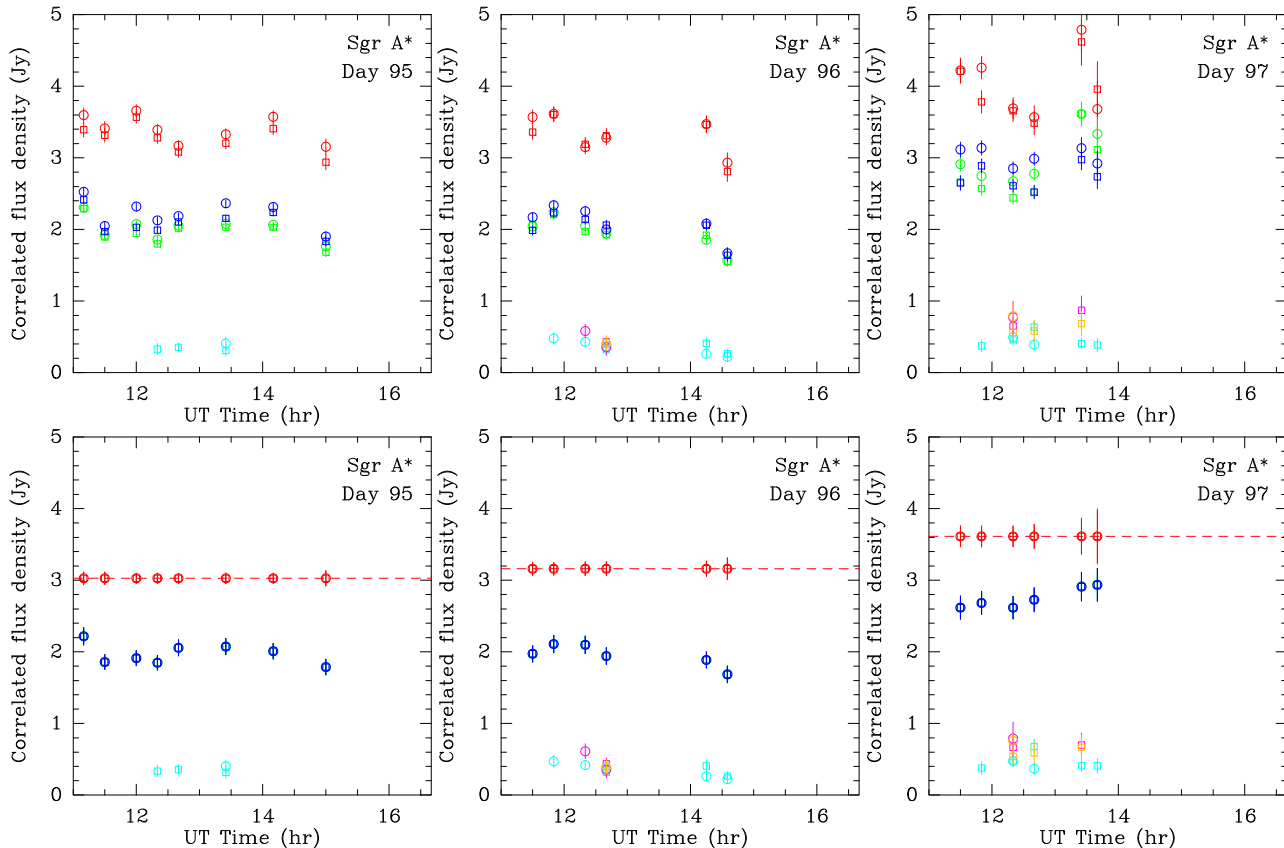
FIG. 2.— Same as Figure 1 but for Sgr A*. Only scans for which detections are seen in both bands on the CD, SC, and SD baselines are shown.

whether a significant correlation exists between the flux density and size of the emission in Sgr A* (Bower et al. 2004; Lu et al. 2010). However, the size of the emission at these wavelengths is dominated by interstellar scattering effects.

Future 1.3 mm VLBI observations with higher sensitivity, sufficient to robustly measure the closure phase, will be an important discriminant between these and other models. For example, an elliptical Gaussian distribution will result in zero closure phase on any triangle of baselines, while a ring model can result in closure phases of 180 degrees depending on the orientation and length of the array baselines. The ring models shown in Figure 3 all have closure phases of zero on the CARMA-ARO/SMT-JCMT triangle of baselines, consistent with the measured closure phases (Section 4). However, a ring model with a null near 3.4 $G\lambda$ between the CARMA-JCMT and ARO/SMT-JCMT baselines, would produce a closure phase of 180 degrees, which is strongly ruled out by the April 2009 data. Measurement on an intermediate baseline in the $1-2\ G\lambda$ range would provide a powerful discriminant between large classes of geometrical models.

5. DISCUSSION

5.1. *Implications for Accretion and Flare Models*

The flux density of Sgr A* on VLBI scales is seen to increase from day 95/96 to day 97. During the first ~ 1 hour on day 97, when the atmosphere at CARMA was relatively stable, the data are consistent with a constant flux density, suggesting that the flux density increased before observations on day 97 but held steady at a higher level than on the previous nights. This behavior is consistent with other (sub)millimeter

observations, which show variability punctuated with periods when the flux density is stable (e.g., Marrone et al. 2006; Yusef-Zadeh et al. 2009; Kunneriath et al. 2010).

The flux density increase appears to be due to an event that establishes a new steady-state in Sgr A*. If instead the flux density increase is due to a short-duration event that concluded before the start of observations on day 97, the unchanging size of the compact region (as implied by Gaussian models in Section 4.2) and the timescale over which the compact flux density is seen to be constant limits the expansion speed of the region to be highly nonrelativistic ($v \lesssim 0.05c$, consistent with Lu et al. 2010) and much lower than the sound speed ($c/\sqrt{3}$) (Marrone et al. 2008), in contrast with relativistic jet models (e.g., Falcke et al. 2009). While a low expansion speed is predicted by adiabatically-expanding plasmon models (Yusef-Zadeh et al. 2009), these models also predict an increase in source size. Our observations detect Sgr A* after the increase in flux density has occurred, but we do not find evidence of an increase in source size as predicted by adiabatic expansion. Future, more sensitive observations of Sgr A* before, during, and after a flare event will be necessary to more fully understand the mechanism responsible for variability in Sgr A*.

5.2. *Physical Models of the Structure of Sgr A**

Numerous physically-motivated models have been advanced to explain the multiwavelength emission from Sgr A* (e.g., Falcke et al. 2000; Yuan et al. 2003; Markoff et al. 2007; Noble et al. 2007). In recent years, several efforts to constrain disk models using 1.3 mm VLBI observations have placed limits on model parameters such as the incli-
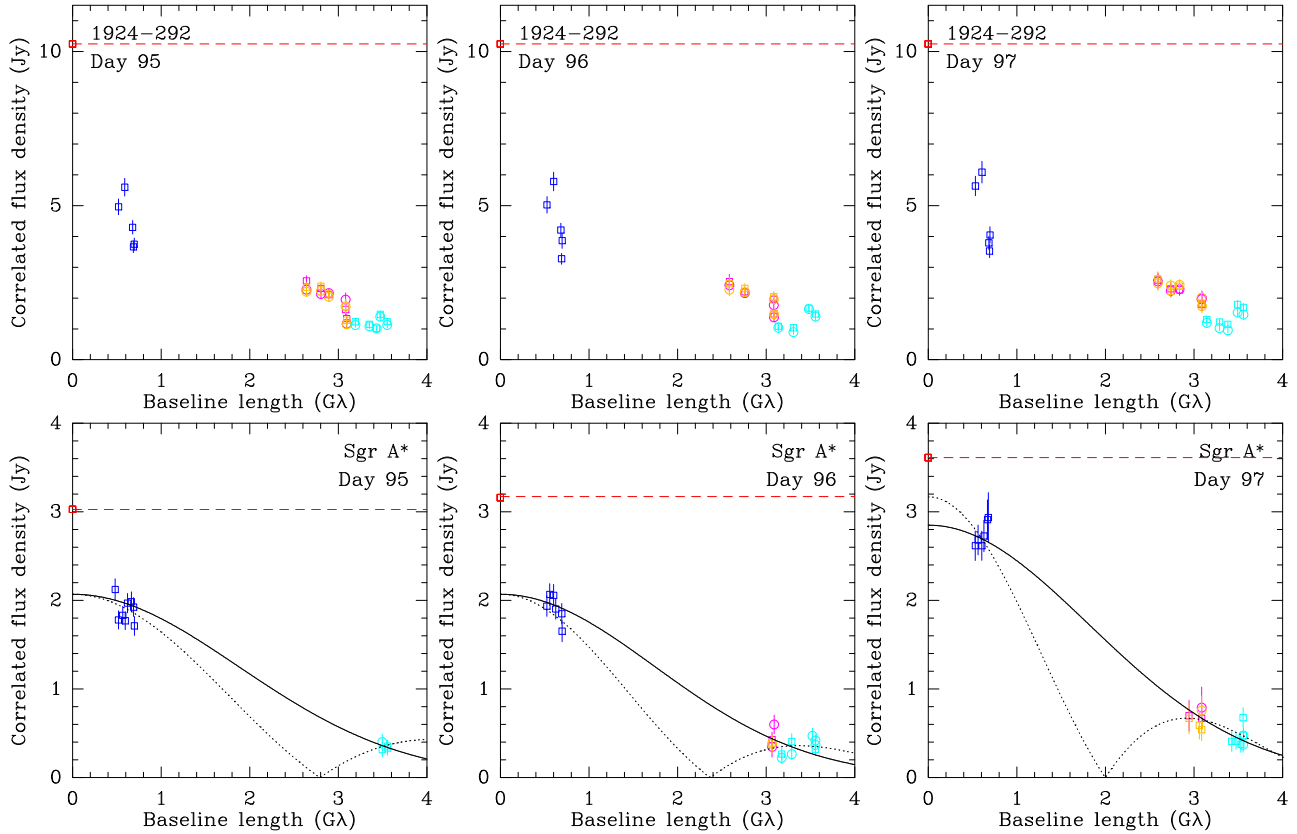
FIG. 3.— Correlated gain-corrected flux density plots. Solid lines show best-fit circular Gaussian models of the compact emission in Sgr A* and are consistent with a source size of approximately 43 μas on all days. The dotted lines show the best ring model fits to Sgr A* data.

nation of the disk and the spin of the black hole. Radiatively inefficient accretion flow models and some general relativistic magnetohydrodynamic simulations found that the Doeleman et al. (2008) data were already sufficient to rule out a low-inclination (i.e., nearly face-on) disk (Broderick et al. 2009; Mościbrodzka et al. 2009). Low-inclination disk models are qualitatively similar to the ring model in Section 4.2, with a "null" in the correlated flux density as a function of baseline length whose depth decreases with increasing disk inclination (Dexter et al. 2009; Fish et al. 2009a). The location of this null as a function of baseline length is set by the ratio of the mass of the black hole and the distance to Sgr A*, which is determined to within a few percent (Ghez et al. 2008; Gillessen et al. 2009).

Emission in high-inclination models is dominated by the highly Doppler-boosted approaching side of the disk. High-inclination disk models exhibit a monotonic decrease in flux density as baselines approach the length of the SJ baseline, with long-baseline correlated flux densities highly dependent on the orientation of the disk in the plane of the sky. The decline of correlated flux density with baseline length from Hawaii-California to Hawaii-Arizona baselines requires that the inclination be $\gtrsim 40°$ in several disk models that were consistent with the 2007 data (Dexter et al. 2009; Broderick et al. 2009). The impact of the 2009 Hawaii-California detections on the 2007 fits is to strengthen the constraint on inclination in these models (e.g., Broderick et al., private communication).

6. SUMMARY

VLBI observations of Sgr A* at 1.3mm wavelength in 2009 have robustly confirmed the detection of Schwarzschild ra-

dius scale structures reported in Doeleman et al. (2008). On the third of three days of observations, the total flux density of Sgr A* was observed to have increased by $\sim 17\%$, indicating an episode of variability similar to those described in multi-wavelength monitoring campaigns (e.g., Marrone et al. 2008; Yusef-Zadeh et al. 2009). The VLBI data support a picture in which this flux density increase is due to a brightening of structure on scales of only a few R_{Sch}. Having achieved the dual technical milestones of successfully detecting closure phase and developing robust methods of amplitude calibration, it is clear that future (sub)millimeter VLBI observations with higher sensitivity and many more baselines will be able to powerfully constrain models of Sgr A* on event horizon scales.

REFERENCES

Bower, G. C., Falcke, H., Herrnstein, R. M., Zhao, J.-H., Goss, W. M., &
    Backer, D. C. 2004, Science, 304, 704
Broderick, A. E., Fish, V. L., Doeleman, S. S., & Loeb, A. 2009, ApJ, 697,
    45
Dexter, J., Agol, E., & Fragile, C. 2009, ApJ, 703, L142
Dodds-Eden, K., et al. 2009, ApJ, 698, 676
Doeleman, S. S., et al. 2001, AJ, 121, 2610
Doeleman, S. S., et al. 2008, Nature, 455, 78
Doeleman, S. S., Fish, V. L., Broderick, A. E., Loeb, A., & Rogers, A. E. E.
    2009, ApJ, 695, 59
Falcke, H., Markoff, S., & Bower, G. C. 2009, A&A, 496, 77
Falcke, H., Melia, F., & Agol, E. 2000, ApJ, 528, 13
Fish, V. L., Broderick, A. E., Doeleman, S. S., & Loeb, A. 2009a, ApJ, 692,
    L14
Fish, V. L., Doeleman, S. S., Broderick, A. E., Loeb, A., & Rogers, A. E. E.
    2009b, ApJ, 706, 1353
Ghez, A., et al. 2008, ApJ, 689, 1044
Gillessen, S., Eisenhauer, F., Trippe, S., Alexander, T., Genzel, R., Martins,
    F., & Ott, T. 2009, ApJ, 692, 1075

Kunneriath, D., et al. 2010, A&A, 517, A46
Lu, R. S., Krichbaum, T. P., Eckart, A., König, S., Kunneriath, D., Witzel,
    G., Witzel, A., & Zensus, J. A. 2010, A&A, in press, arXiv:1010.1287
Markoff, S., Bower, G. C., & Falcke, H. 2007, MNRAS, 379, 1519
Marrone, D. P., Moran, J. M., Zhao, J.-H., & Rao, R. 2006, ApJ, 640, 308
Marrone, D. P., et al. 2008, ApJ, 682, 373
Mościbrodzka, M., Gammie, C. F., Dolence, J. C., Shiokawa, H., & Leung,
    P. K. 2009, ApJ, 706, 497
Noble, S. C., Leung, P. K., Gammie, C. F., & Book, L. G. 2007, Classical
    and Quantum Gravity, 24, 259
Reid, M. 2009, International Journal of Modern Physics D, 18, 889
Rogers, A. E. E., Doeleman, S. S., & Moran, J. M. 1995, AJ, 109, 1391
Shen, Z. -Q., et al. 1997, AJ, 114, 1999
Yuan, F., Quataert, E., & Narayan, R. 2003, ApJ, 598, 301
Yusef-Zadeh, F., et al. 2009, ApJ, 706, 348

TABLE 1
GAIN-CORRECTED DETECTIONS OF 1924−292 AND SGR A*

Source	Day Number	UT Time (hh mm)	Baseline	Band	u (Mλ)	v (Mλ)	Flux Density (Jy)	σ (Jy)
1924−292	95	13 10	SC	both	-509	105	4.96	0.26
			SJ	low	-3103	-1561	1.47	0.11
			SJ	high	-3103	-1561	1.40	0.12
			JC	low	2594	1667	1.63	0.19
			JC	high	2594	1667	1.95	0.22
			JD	low	2594	1667	1.72	0.20
			JD	high	2594	1667	1.73	0.22
		13 55	SC	both	-569	157	5.60	0.29
			SJ	low	-3325	-1251	1.24	0.09
			SJ	high	-3325	-1251	1.13	0.09
			JC	low	2756	1408	1.33	0.14
			JC	high	2756	1408	1.17	0.14
			JD	low	2756	1408	1.28	0.14
			JD	high	2756	1408	1.15	0.14
		15 25	SC	both	-621	273	4.30	0.22
			SJ	low	-3380	-598	1.02	0.07
			SJ	high	-3380	-598	1.02	0.07
			JC	low	2759	871	2.11	0.13
			JC	high	2759	871	2.16	0.13
			JD	low	2759	871	2.13	0.13
			JD	high	2759	871	2.04	0.12
		15 45	SC	both	-619	300	3.66	0.19
			SJ	low	-3320	-454	1.15	0.07
			SJ	high	-3320	-454	1.08	0.07
			JC	low	2701	754	2.31	0.14
			JC	high	2701	754	2.13	0.13
			JD	low	2701	754	2.38	0.15
			JD	high	2701	754	2.23	0.14
		16 15	SC	both	-608	339	3.75	0.20
			SJ	low	-3184	-246	1.23	0.08
			SJ	high	-3184	-246	1.12	0.07
			JC	low	2575	585	2.56	0.16
			JC	high	2575	585	2.27	0.15
			JD	low	2576	585	2.35	0.15
			JD	high	2576	585	2.21	0.15
	96	13 10	SC	both	-515	110	5.03	0.27
			SJ	low	-3127	-1535	1.67	0.12
			SJ	high	-3127	-1535	1.64	0.12
			JC	low	2612	1645	1.96	0.16
			JC	high	2612	1645	1.77	0.16
			JD	low	2612	1645	2.04	0.17
			JD	high	2612	1645	1.96	0.17
		14 00	SC	both	-578	168	5.78	0.30
			SJ	low	-3354	-1187	1.48	0.10
			SJ	high	-3354	-1187	1.40	0.10
			JC	low	2776	1356	1.48	0.13
			JC	high	2776	1356	1.38	0.12
			JD	low	2776	1356	1.47	0.13
			JD	high	2776	1356	1.47	0.13
		15 30	SC	both	-621	285	4.21	0.22
		15 50	SC	both	-617	312	3.28	0.18
			SJ	low	-3286	-391	1.04	0.07
			SJ	high	-3286	-391	0.90	0.07
			JC	low	2668	703	2.21	0.15

TABLE 1
GAIN-CORRECTED DETECTIONS OF 1924−292 AND SGR A*

			JC	high	2668	703	2.16	0.15
			JD	low	2668	703	2.32	0.15
			JD	high	2668	703	2.19	0.15
		16 20	SC	both	-603	351	3.86	0.25
			SJ	low	-3132	-185	1.09	0.13
			SJ	high	-3132	-185	1.04	0.10
			JC	low	2529	536	2.54	0.23
			JC	high	2529	536	2.41	0.21
			JD	low	2529	536	2.46	0.22
			JD	high	2529	536	2.27	0.19
	97	13 10	SC	both	-521	114	5.64	0.32
			SJ	low	-3151	-1509	1.79	0.14
			SJ	high	-3151	-1509	1.53	0.12
			JC	low	2630	1623	1.79	0.20
			JC	high	2630	1623	2.00	0.23
			JD	low	2630	1623	1.80	0.21
			JD	high	2630	1623	1.74	0.21
		14 00	SC	both	-582	173	6.09	0.35
			SJ	low	-3365	-1159	1.70	0.13
			SJ	high	-3365	-1159	1.47	0.11
			JC	low	2783	1332	1.81	0.19
			JC	high	2783	1332	1.97	0.22
			JD	low	2783	1332	1.83	0.20
			JD	high	2783	1332	2.01	0.23
		15 30	SC	both	-620	290	3.79	0.21
			SJ	low	-3344	-505	1.15	0.08
			SJ	high	-3344	-505	0.95	0.07
			JC	low	2724	796	2.27	0.18
			JC	high	2724	796	2.29	0.18
			JD	low	2724	796	2.39	0.17
			JD	high	2724	796	2.43	0.18
		15 50	SC	both	-616	317	3.53	0.21
			SJ	low	-3269	-364	1.23	0.09
			SJ	high	-3269	-364	1.03	0.08
			JC	low	2653	681	2.30	0.20
			JC	high	2653	681	2.24	0.20
			JD	low	2653	681	2.22	0.19
			JD	high	2653	681	2.41	0.19
		16 15	SC	both	-604	349	4.05	0.27
			SJ	low	-3139	-193	1.31	0.11
			SJ	high	-3139	-193	1.20	0.11
			JC	low	2535	542	2.58	0.23
			JC	high	2535	542	2.54	0.25
			JD	low	2535	542	2.63	0.23
			JD	high	2535	542	2.48	0.23
Sgr A*	95	11 10	SC	both	-474	85	2.22	0.13
		11 30	SC	both	-507	106	1.86	0.11
		12 00	SC	both	-550	140	1.91	0.11
		12 20	SC	both	-573	164	1.85	0.10
			SJ	low	-3338	-1222	0.33	0.08
		12 40	SC	both	-591	188	2.06	0.11
			SJ	low	-3391	-1080	0.36	0.07
		13 25	SC	both	-617	246	2.07	0.11
			SJ	low	-3414	-754	0.32	0.08
			SJ	high	-3414	-754	0.40	0.09
		14 10	SC	both	-618	305	2.01	0.11
		15 00	SC	both	-592	370	1.79	0.11
	96	11 30	SC	both	-513	110	1.98	0.12
		11 50	SC	both	-542	133	2.11	0.12
			SJ	high	-3231	-1404	0.47	0.08
		12 20	SC	both	-577	168	2.10	0.13
			SJ	high	-3350	-1195	0.42	0.07
			JC	high	2774	1363	0.61	0.11
		12 40	SC	both	-595	193	1.95	0.12
			SJ	low	-3398	-1051	0.32	0.06
			SJ	high	-3398	-1051	0.37	0.06
			JC	low	2804	1245	0.44	0.09
			JC	high	2804	1245	0.35	0.12
			JD	low	2804	1245	0.40	0.09
			JD	high	2804	1245	0.39	0.10
		14 15	SC	both	-616	317	1.89	0.12
			SJ	low	-3269	-370	0.41	0.09
			SJ	high	-3269	-370	0.26	0.06
		14 35	SC	both	-607	343	1.69	0.12
			SJ	low	-3168	-233	0.27	0.07
			SJ	high	-3168	-233	0.22	0.06
	97	11 30	SC	both	-519	115	2.62	0.17

Fish et al.

TABLE 1
GAIN-CORRECTED DETECTIONS OF 1924−292 AND SGR A*

11 50	SC	both	-547	137	2.68	0.17
	SJ	low	-3250	-1377	0.38	0.09
12 20	SC	both	-581	173	2.62	0.16
	SJ	low	-3362	-1167	0.48	0.08
	SJ	high	-3362	-1167	0.48	0.08
	JC	low	2781	1340	0.67	0.13
	JC	high	2781	1340	0.79	0.23
	JD	low	2781	1340	0.54	0.12
	JD	high	2781	1340	0.76	0.17
12 40	SC	both	-598	198	2.73	0.18
	SJ	low	-3404	-1023	0.68	0.11
	SJ	high	-3404	-1023	0.37	0.08
	JD	low	2807	1221	0.59	0.16
13 25	SC	both	-619	257	2.91	0.22
	SJ	low	-3405	-697	0.41	0.09
	JC	low	2786	953	0.70	0.17
	JD	low	2786	953	0.67	0.17
13 40	SC	both	-621	276	2.94	0.28
	SJ	low	-3375	-589	0.41	0.11

TABLE 2
MODEL FITS TO SGR A* DATA

Model	Day Number	Compact Flux Density (Jy)	Inner Size (μas)	Outer Size (μas)
Gaussian	95	2.07	41	$\cdots$
	96	2.07	44	$\cdots$
	97	2.85	43	$\cdots$
Ring	95	2.07	53	60
	96	2.07	37	92
	97	3.17	48	106